Journal of Industrial and Engineering Chemistry 68 (2018) 109–116

Contents lists available at ScienceDirect

Journal of Industrial and Engineering Chemistry

journal homepage: www.elsevier.com/locate/jiec

Exploration of structural, thermal and spectroscopic properties of self-activated sulfate $Eu_2(SO_4)_3$ with isolated SO_4 groups

Yu.G. Denisenko[a,b], A.S. Aleksandrovsky[c,d], V.V. Atuchin[e,f,*], A.S. Krylov[g], M.S. Molokeev[h,i,j], A.S. Oreshonkov[g,i], N.P. Shestakov[g], O.V. Andreev[a]

[a] Institute of Chemistry, Tyumen State University, Tyumen 625003, Russia
[b] Department of General and Special Chemistry, Industrial University of Tyumen, Tyumen 625000, Russia
[c] Laboratory of Coherent Optics, Kirensky Institute of Physics Federal Research Center KSC SB RAS, Krasnoyarsk 660036, Russia
[d] Institute of Nanotechnology, Spectroscopy and Quantum Chemistry, Siberian Federal University, Krasnoyarsk 660041, Russia
[e] Laboratory of Optical Materials and Structures, Institute of Semiconductor Physics, SB RAS, Novosibirsk 630090, Russia
[f] Laboratory of Semiconductor and Dielectric Materials, Novosibirsk State University, Novosibirsk 630090, Russia
[g] Laboratory of Molecular Spectroscopy, Kirensky Institute of Physics Federal Research Center KSC SB RAS, Krasnoyarsk 660036, Russia
[h] Laboratory of Crystal Physics, Kirensky Institute of Physics, Federal Research Center KSC SB RAS, Krasnoyarsk 660036, Russia
[i] Siberian Federal University, Krasnoyarsk 660041, Russia
[j] Department of Physics, Far Eastern State Transport University, Khabarovsk 680021, Russia

ARTICLE INFO

Article history:
Received 14 May 2018
Received in revised form 5 July 2018
Accepted 24 July 2018
Available online 1 August 2018

Keywords:
Europium sulfate
Synthesis
Structure
Thermal analysis
Photoluminescence

ABSTRACT

$Eu_2(SO_4)_3$ was synthesized by chemical precipitation method and the crystal structure was determined by Rietveld analysis. The compound crystallizes in monoclinic space group C2/*c*. In the air environment, $Eu_2(SO_4)_3$ is stable up to 670 °C. The sample of $Eu_2(SO_4)_3$ was examined by Raman, Fourier-transform infrared absorption and luminescence spectroscopy methods. The low site symmetry of SO_4 tetrahedra results in the appearance of the IR inactive ν_1 mode around 1000 cm^{-1} and ν_2 modes below 500 cm^{-1}. The band intensities redistribution in the luminescent spectra of Eu^{3+} ions is analyzed in terms of the peculiarities of its local environment.

Introduction

Sulfates are well known compounds in chemistry and mineralogy, and they are of great importance for human life, urban technology, industry and environmental stability [1–6]. Sulfate chemistry has been developed since ancient times and a lot of inorganic and organic–inorganic compounds were synthesized and evaluated [2,6–9]. However, the history of rare earth (Ln) sulfates is comparatively short and significant properties of the crystals remain unknown because many compounds are difficult in their synthesis and storage due to active hydration in contact with the humid air. There is very scarce information about the crystal structure of Ln elements anhydrous sulfates $Ln_2(SO_4)_3$. Up to now, for the partial set of Ln = La–Gd, excluding Pm, the monoclinic crystal structure in space group *C*2/*c* was only defined for $Nd_2(SO_4)_3$ [10]. For the $Ln_2(SO_4)_3$ compounds, Ln = La, Ce, Pr, Sm, Eu, Gd, the structures were not solved and only the monoclinic unit cell parameters were obtained *via* the structural analogy to $Nd_2(SO_4)_3$ [11–15]. For an observation, the known structural characteristics are summarized in Table S1. As to the partial set of Ln = Y, Tb–Lu, the orthorhombic structures in space group *Pbcn* were determined for sulfates $Ln_2(SO_4)_3$, Ln = Y, Er [16–18]. Besides, the orthorhombic structure type of anhydrous sulfates was verified for Ln = Tb, Dy, Ho, Tm, Yb and Lu [19,20], and trigonal structures were determined for β-$Yb_2(SO_4)_3$ and closely related sulfate $Sc_2(SO_4)_3$ [16,21]. Thus, it can be mentioned that several structure types are possible in sulfates $Ln_2(SO_4)_3$ depending on the rare earth element selection. Above this, the existence of polymorphic modifications was reported on for $Yb_2(SO_4)_3$ [20,21].

Among rare earth compounds, the crystals carrying Eu^{3+} ions are of particular interest because the ions originate efficient red photoluminescence appropriate for the creation of WLED devices with spectral properties similar to the Sun daylight. In the recent years, the spectroscopic properties of different Eu^{3+}-bearing phosphors were evaluated to see the relation between their structural and optical characteristics [22–26]. However, in the phosphor compounds, the Eu^{3+} doping level is commonly low and,

* Corresponding author at: Institute of Semiconductor Physics, Novosibirsk 630090, Russia.
E-mail address: atuchin@isp.nsc.ru (V.V. Atuchin).

https://doi.org/10.1016/j.jiec.2018.07.034
1226-086X/

frequently, the Eu^{3+} ions distribution over the appropriate crystallographic positions is not evident. For this reason, in complex compounds, it is difficult to define clearly the relation between the spectroscopic parameters and the Eu^{3+} ion coordination in the host lattice. In this situation, the europium compounds, where Eu^{3+} is a constituent element, are more suitable for this purpose because the Eu^{3+} ion coordination can be precisely defined by the methods of modern crystal structure analysis [27–34]. Thus, the present study is aimed at the synthesis of anhydrous $Eu_2(SO_4)_3$ and evaluation of their structural and optical properties. As it is well known, the S—O bonds are very short and it is particularly interesting to see the spectroscopic parameters of Eu^{3+} ions in the SO_4 tetrahedral environment.

In the past, several studies were devoted to the synthesis and characterization of europium (III) sulfate, and it was shown that the preparation of $Eu_2(SO_4)_3$ is a nontrivial task because of high a tendency to hydration [13,35–38]. The available structural properties of the presently known Eu^{3+} sulfate hydrates are listed in Table S2 [20,35,39–43]. Nevertheless, to the best of our knowledge, the crystal structure and basic physical properties of anhydrous $Eu_2(SO_4)_3$ are still unknown. To fill this gap, in the present work, the polycrystalline powder of $Eu_2(SO_4)_3$ has been synthesized and the crystal structure of the sulfate has been determined for the first time. It might be well to point that much research on synthesis of materials for various applications by different methods, including the green chemistry approach, were conducted recently [44–63]. However, to provide synthesis of stoichiometric $Eu_2(SO_4)_3$ compound, the precipitation approach was used in the present study. Then, the thermal and spectroscopic characteristics of the compound were evaluated in detail and compared to those of monoclinic α-$Eu_2(MoO_4)_3$ which structure is closely related to that of $Eu_2(SO_4)_3$.

Experimental methods

The $Eu_2(SO_4)_3$ powder was obtained by precipitation from a solution of europium nitrate by concentrated sulfuric acid. The high purity starting reagents were used for synthesis: Eu_2O_3 (99.99%, ultrapure, TDM-96 Ltd. Russia), concentrated nitric acid solution ($C(HNO_3) = 14.6$ mol/l, ultrapure, Vekton Ltd., Russia), concentrated sulfuric solution acid ($C(H_2SO_4) = 17.9$ mol/l, ultrapure, Vekton Ltd., Russia). In the acids used, the metal cation content does not exceed 0.000321% for H_2SO_4 and 0.000041% for HNO_3. Concentration of acid solutions was established by alkalimetry using NaOH as the working solution ($C = 0.1$ mol/l). Weighing the dry reagents was carried out on an analytical balance with an accuracy of 0.1 mg. The bulk reagents were weighed into glass bins with ground lid. Prior to weighing, europium oxide was calcined in a muffle furnace at the temperature of 1000 °C for 12 h to remove the gases adsorbed from the air and the products of their interaction with the Eu_2O_3 oxide surface. The acid solutions were measured off by means of glass measuring cylinders at the accuracy of 0.1 ml. We refused to use automatic dispensers due to possible corrosion.

Initially, the 5.00 g Eu_2O_3 charge was placed in a 100 ml glass round-bottomed flask. Then, 6.1 ml of the concentrated nitric acid solution were added in small portions. The reaction mixture was heated with a continuous stirring until the oxide was completely dissolved. It may be necessary to heat the reaction mixture. As a result, the europium(III) nitrate solution was obtained by reaction:

$$Eu_2O_3 + 6HNO_3 \rightarrow 2Eu(NO_3)_3 + 3H_2O$$

When working with concentrated sulfuric acid, special care must be taken. Its addition to the aqueous solution of nitrate causes a strong warming up of the reaction mixture up to its boiling point. After cooling the solution, 2.6 ml (an excess of 10%) of the concentrated sulfuric acid solution were added to the flask in small portions, not allowing a strong reheating of the reaction mixture. The reaction mixture, during the addition of sulfuric acid, must be stirred with a glass stirrer, at a speed of 300 rpm. The reaction results in the europium sulfate precipitation:

$$2Eu(NO_3)_3 + 3H_2SO_4 \rightarrow Eu_2(SO_4)_3\downarrow + 6HNO_3$$

In no case should metal products be allowed to contact with the reaction mixtures at the acid treatment stages, as this can lead to a change in the cation composition of the synthesized product. In reactions without heating, fluoroplastic laboratory glassware can be used. In all other cases, only glass should be applied.

After the precipitation, the mixture was distilled to a dry residue. The europium sulfate powder was additionally calcined in a tubular furnace at the temperature of 500 °C to remove the adsorbed acid and then annealed in a muffle furnace at the same temperature for 7 days to form the final powder product.

As a result of all the above manipulations, a polycrystalline product with a mass of 8.3976 g was obtained, which is 99.82% of the theoretical yield. This fact makes it possible to characterize the method as highly efficient. According to the gravimetric analysis, the content of sulfate ions in the synthesized product was 48.66% and the theoretical value is 48.65% for $Eu_2(SO_4)_3$.

This method of rare earth sulfates synthesis has several significant advantages:

- During the synthesis, no other metal cations, except Eu^{3+}, are introduced into the reaction mixture and this excludes its substitution in the crystal lattice and the double salt formation.
- Europium sulfate is precipitated from a homogeneous solution of europium nitrate, which ensures a high stoichiometry of the sample.
- The reaction in a concentrated sulfuric acid environment provides the anhydrous sulphate structure formation and suppresses the crystalline hydrates generation even at very early precipitation stages.

Under the Sun daylight illumination, the synthesized $Eu_2(SO_4)_3$ powder possesses light-cream tint, as seen in Fig. 1, that is a common characteristic of oxide compounds of trivalent europium [28,34,64].

The powder diffraction data of $Eu_2(SO_4)_3$ for the Rietveld analysis were collected at room temperature with a Bruker D8 ADVANCE powder diffractometer (Cu-Kα radiation) and linear VANTEC detector. The step size of 2θ was 0.016°, and the counting

Fig. 1. The digital image of $Eu_2(SO_4)_3$ powder under the Sun day illumination.

time was 2.5 s per step. The 2θ range of 7.5–70° was measured with a 0.6 mm divergence slit, but the 2θ range of 70–140° was measured with a 2 mm divergence slit. The larger slits allow a noticeable intensity increase for higher-angle peaks without a resolution decrease because the higher-angle peaks are broad enough to be not affected by a bigger divergence beam. The esd's $\sigma(I_i)$ of all points on the patterns were calculated using intensities I_i: $\sigma(I_i) = I_i^{1/2}$. The intensities and obtained esd values were further normalized *via* relations $I_{i\,norm} = I_i \times 0.6/(\text{slit width})$, $\sigma_{norm}(I_i) = \sigma(I_i) \times 0.6/(\text{slit width})$, taking into account the actual value of the divergence slit width which was used to measure each particular intensity I_i, and was saved in the xye-type file. In this algorithm, the transformed diffraction pattern has a usual view over the whole 2θ range of 7.5–140°, but all high-angle points have small esd values.

Scanning Electron Microscopy (SEM) was carried out on electron microscope JEOL JSM-6510LV. X-ray energy-dispersive analyzer Oxford Instruments X-Max 20 mm^2 was used to register X-rays at element spectrum plotting in selected sample surface areas. The chemical composition measurements were carried out with the use of a pressed tablet. The inaccuracy in the element content determination was equal to ±0.2%. The thermal analysis was carried out in the argon flow at Simultaneous Thermal Analysis (STA) equipment 499 F5 Jupiter NETZSCH (Germany). The powder samples were inserted into alumina crucibles. The heating rate was 3 °C/min. For the enthalpy determination, the equipment was initially calibrated with the use of standard metal substances, such as In, Sn, Bi, Zn, Al, Ag, Au, Ni. The heat effect peaks were determined with package "Proteus 6 2012". The peak temperatures and areas in parallel experiments were reproduced at an inaccuracy lower than 3%.

The unpolarized Raman spectra were collected in a backscattering geometry, using a triple monochromator Horiba Jobin Yvon T64000 Raman spectrometer operating in the subtractive mode and then detected by an LN-cooled charge-coupled device. The spectral resolution for the recorded Stokes side Raman spectra was set to ~2.5 cm^{-1} (this resolution was reached by using gratings with 1800 grooves/mm and 100 mm slits). The microscope system, based on the Olympus BX41 microscope with an Olympus 50× objective lens f = 0.8 mm with NA = 0.75 numerical aperture, provides a focal spot diameter of about 3 μm on the sample [66,67]. Single-mode argon 457.9 nm line from a Spectra-Physics Stabilite 2017 Ar^+ laser of 1 mW on the sample was used as an excitation light source. The laser light intensity was adjusted to avoid the sample heating. The vacuum Fourier-transform spectrometer VERTEX 70 V (BRUKER) was used to obtain the IR (infrared) absorption spectra with spectral resolution 4 cm^{-1}. The spectrum was produced from the sample shaped as about 0.4 mm thick tablet of 13 mm in diameter. The tablet was prepared as follows: 0.003 g of $Eu_2(SO_4)_3$ was thoroughly ground with 0.111 g of KBr. The force equal to ten tons was applied at the produced mixture. The Globar was used as an IR radiation source, and it was equipped with a KBr wide beamsplitter and RT-DLaTGS as a detector. The high resolution luminescence spectra under the room temperature were registered on a Horiba Jobin Yvon T64000 Raman spectrometer.

Results and discussion

The X-ray diffraction pattern recorded for $Eu_2(SO_4)_3$ is shown in Fig. 2. The compound crystallizes in the monoclinic structure, space group C2/*c*. The Rietveld refinement was performed using a TOPAS 4.2 package which accounts the esd's of each point by a special weight scheme [65]. All peaks were indexed by the monoclinic unit cell (C2/*c*) with the parameters close to those of $Nd_2(SO_4)_3$ [10] and, therefore, this crystal structure was taken as a starting model for the Rietveld refinement. However, the

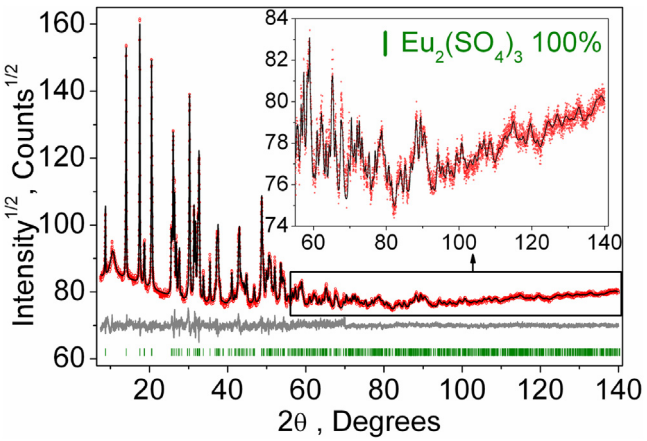

Fig. 2. The measured (red), calculated (black) and differential (blue) diffraction patterns of $Eu_2(SO_4)_3$. (For interpretation of the references to color in this figure legend, the reader is referred to the web version of this article).

nonstandard space group *B*2/*b* used earlier [10] was transformed into a standard setting C2/*c* and all atom coordinates were transformed accordingly. Respectively, the Nd^{3+} sites in the $Nd_2(SO_4)_3$ structure were assumed as occupied by Eu^{3+} ions in the $Eu_2(SO_4)_3$ structure. To reduce the number of refined parameters, only one thermal parameter was refined for all O atoms. The refinement was stable and it gave low *R*-factors. The main crystallographic parameters obtained for $Eu_2(SO_4)_3$ are listed in Table 1, and the atom coordinates and bond lengths are summarized in Tables S3 and S4, respectively.

The $Eu_2(SO_4)_3$ structure is shown in Fig. 3. In the structure, the Eu^{3+} ion is surrounded by seven sulfate groups, two of which are chelating groups, and, therefore, the general coordination number of europium in the structure is equal to nine. The coordination polyhedron is a deformed three-cap trigonal prism. The coordination polyhedra are banded in pairs by the surfaces that consisted of three oxygen atoms and the polyhedra formed the chains parallel to axis c. The bonding of chains with parallel layers of crystallographically different sulfate groups leads to the formation of a three-dimensional framework crystal structure. The topological analysis of the net by Topos Pro program [68], using the simplification that Eu^{3+} and both SO_4^{2-}tetrahedral groups are nodes, revealed that this is a 3-nodal (4-c)(5-c)$_2$(9-c)$_2$ net with point symbol $(3^2 \cdot 4^2 \cdot 5^2)(3^2 \cdot 4^7 \cdot 5)_2(3^6 \cdot 4^{14} \cdot 5^8 \cdot 6^8)_2$, which is new. In the coordinated polyhedron the lengths of eight Eu—O bonds are in the range of 2.30–2.58 Å. One bond has the length of 2.80 Å that allow identifing the coordination number of europium in the structure as 8 + 1. In comparison, the Nd—O bond lengths in $Nd_2(SO_4)_2$ are in the range of 2.32–2.69 Å and the ninth longest

Table 1
Main $Eu_2(SO_4)_3$ sample processing and refinement parameters.

Compound	$Eu_2(SO_4)_3$
Sp.Gr.	*C*2/*c*
a, Å	21.2787 (8)
b, Å	6.6322 (3)
c, Å	6.8334 (3)
β, °	108.002 (2)
V, Å^3	917.16 (6)
Z	4
2*θ*-interval, °	7.5–140
R_{wp}, %	1.31
R_p, %	1.18
R_{exp}, %	0.84
χ^2	1.56
R_B, %	0.59

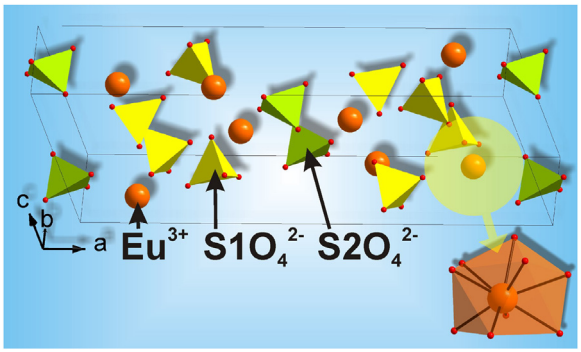

Fig. 3. The crystal structure of $Eu_2(SO_4)_3$. The unit cell is outlined. Lone oxygen atoms are omitted for clarity.

bond length is 2.75 Å. Since Nd—O bond lengths are closer to each other, the distortion index ($D = (1/n)\sum((L_i - <L>)/<L>)$ [69], where L_i is the distance from the central atom to the ith coordinating atom and <L> is the average bond length), the value D = 0.042 is slightly smaller than that of the $Eu_2(SO_4)_2$ compound having D = 0.046 [49].

There are two independent sulfate tetrahedra in the asymmetric part of the unit cell. In the first type of tetrahedra, two oxygen atoms are coordinated by two europium atoms in pairs. Herewith, one europium atom is chelately bonded and the other one is monodentately bonded. In the second type of tetrahedra, two oxygen atoms are monodentately bonded with two europium atoms. The other two oxygen atoms are bonded with three europium atoms: one is chelately bonded and two are monodentately bonded. In both tetrahedra, the O—S—O angles are different from the ideal tetrahedral angle and vary within 102–121°, and that leads to a significant deforming of tetrahedra. The sulfate tetrahedra in europium(III) sulfate have much more deformation in comparison with the tetrahedra in the structures of europium sulfates crystallohydrates [20,35,39–43], apparently, because of a higher anhydrous sulfate structure rigidity.

The representative SEM pattern recorded for the $Eu_2(SO_4)_3$ powder is shown in Fig. 4. According to the SEM observation, the obtained europium sulfate product is mostly formed by unfaceted particles of 1–50 μm in size. As it is evident in Fig. S1, the sample contains only constituent elements Eu, S and O. The obtained element ratio averaged for 5 measurements Eu:S:O = 51.32:16.25:32:43 is in excellent relation to nominal composition Eu:S:O = 51.33:16.25:32:42. As evident in Fig. S2, the constituent element distributions over the sample surface are very uniform.

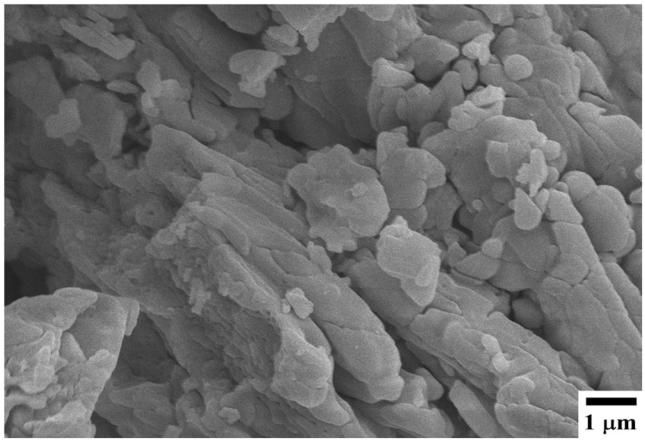

Fig. 4. SEM pattern of $Eu_2(SO_4)_3$ powder.

To see the thermal stability range for $Eu_2(SO_4)_3$, the TG/DSC measurements were implemented. It is well known, that rare earth salts precipitation from aqueous solutions inevitably leads to the formation of a mixture of crystalline hydrates [70,71]. Then, the main problems in the anhydrous salts formation by the thermal decomposition of their crystalline hydrates are the complete removal of all crystalline hydrate water molecules and the absence of pyrohydrolysis processes [72,73]. The oxidation and pyrohydrolysis of inorganic salts commonly proceed with the heat development [74,75]. Respectively, the pyrohydrolysis processes of $Eu_2(SO_4)_3$ can be described by the following chemical equations:

$$Eu_2(SO4)_{3(s)} + 2H_2O_{(g)} \rightarrow Eu_2O_2SO_{4(s)} + 2H_2SO_{4(l)} \quad (1)$$

$$Eu_2(SO_4)_{3(s)} + 3H_2O_{(g)} \rightarrow Eu_2O_{3(s)} + 3H_2SO_{4(l)} \quad (2)$$

The reaction enthalpies can be calculated using the formation enthalpies of the starting and resulting compounds [38,76–78]. The values are equal to −393.8 and −290.3 kJ/mol for reactions (1) and (2), respectively. This means that the pyrohydrolysis processes should proceed with a drastic development of heat.

For the investigation of these issues, the highest crystalline hydrate of europium sulfate $Eu_2(SO_4)_3 \cdot 8H_2O$ (home made) was chosen as a starting point. The related XRD pattern is shown in Fig. S3(a). The TG/DSC curves recorded for the of $Eu_2(SO_4)_3 \cdot 8H_2O$ sample are shown in Fig. 5. According to the DTA data, the thermal dehydration of europium sulfate hydrate proceeds in one step and it is completed at ~350 °C. The phase transformation over the range of 25–350 °C is accompanied by a strong endothermic effect, which indicates the absence of pyrohydrolysis processes. According to the TG data, the composition of the product existing in the temperature range of 350–670 °C is well described by formula $Eu_2(SO_4)_3$. The heat development effect at ~400 °C is not accompanied by a mass change and it could be interpreted as the crystallization of an amorphous component appeared in the dehydration process [38]. According to the TG data, the $Eu_2(SO_4)_3$ decomposition associated with the sulfate group destruction begins from ~670 °C. The product of this process is europium oxysulfate $Eu_2O_2SO_4$, as verified by the XRD analysis shown in Fig. S3(c) [79]. The final thermal decomposition product of $Eu_2(SO_4)_3 \cdot 8H_2O$ is europium oxide Eu_2O_3 formed at ~1170 °C. For each crystaline phase observed in the TG/DSC experiment, the particle size was estimated using package TOPAS 4.2 and the results are summarized in Table 2. Thus, the temperature of ~500 °C chosen in the present study for the precipitate calcination is optimal for reaching anhydrous europium sulfate $Eu_2(SO_4)_3$. This temperature is high enough to decompose all the formed crystalline hydrates, but it is not too high to initiate of the thermal destruction process of $Eu_2(SO_4)_3$.

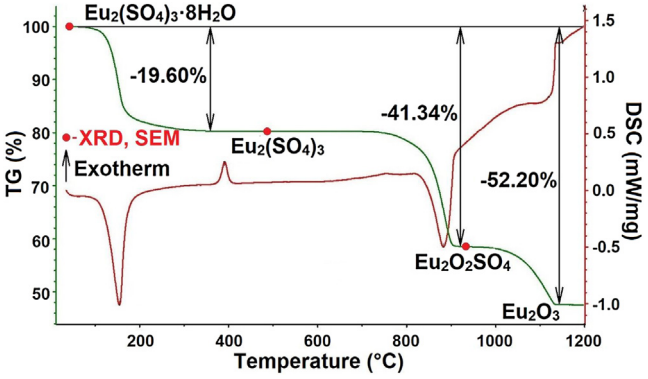

Fig. 5. TG/DSC of $Eu_2(SO_4)_3$.

Table 2
Particle size values obtained for Eu-containing compounds.

Compound	$Eu_2(SO_4)_3$	$Eu_2(SO_4)_3{\cdot}8(H_2O)$	$Eu_2O_2SO_4$
Average crystal size, nm	64.4(4)	69(1)	89(1)

The peaks broadening caused by the temperature increase was registered in the thermogram. This fact indicates a kinetic complication of high-temperature processes in comparison with low-temperature processes. According to the available kinetic data, calculated by the Kissinger equation, the energy activation barrier strongly increases during the transition from the dehydration of the crystalline hydrate (Ea = 71 kJ/mol) to the decomposition of sulfates $Eu_2(SO_4)_3$ (Ea = 303 kJ/mol) and $Eu_2O_2SO_4$ (Ea = 400 kJ/mol), although somewhat offset by an increase in the pre-exponential factor, which, in fact, reflects an increase in the usefulness of the steric factor of activation entropy [38]. Obviously, the kinetic difficulties that appeared with the $Eu_2(SO_4)_3 \cdot 8H_2O$ dehydration are the least. The reduced rigidity of the structure facilitates this process passing.

In our opinion, the pre-exponential factor in the processes of thermal destruction of salt systems, not related to the collision of molecules, depends on the symmetry of the polyhedra in the structure. In order to initiate thermal decomposition, a needed condition is that the polyhedra, in the result of thermal oscillations, undergo that kind of deformation that makes their further existence impossible. Consequently, the structures with the highest structural element symmetry will show the greatest kinetic stability on the temperature increase. Such structures will be characterized by a large value of the pre-exponential factor as a steric factor associated with the structure symmetry.

The crystal structures of $Eu_2(SO_4)_3$ and $Eu_2O_2SO_4$ [79] are represented by the identical structural elements: three-capped trigonal prisms [EuO_9] and tetrahedra [SO_4]. The polyhedra in the $Eu_2O_2SO_4$ structure are characterized by their lower distortion due to the presence of bridging oxygen atoms μ-O, and the structure exhibits a greater kinetic stability by experiencing a lower deformation stress.

The Raman and IR spectra obtained for $Eu_2(SO_4)_3$ are shown in Figs. 6 and 7, respectively. The vibrational representation for the monoclinic phase of $Eu_2(SO_4)_3$ at the Brillouin zone center is: $\Gamma_{vibr} = 25A_g + 26B_g + 25A_u + 26B_u$. The odd modes $\Gamma_{acoustic} = A_u + 2B_u$ are acoustic ones while remaining modes are optical. A_g and B_g

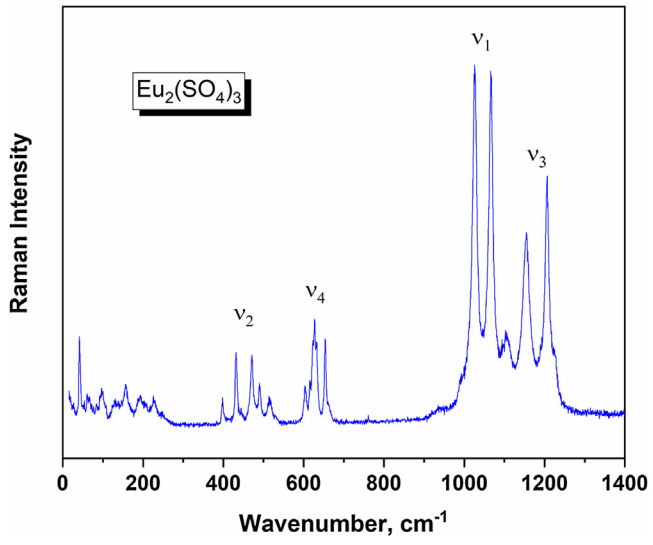

Fig. 6. The Raman spectrum of $Eu_2(SO_4)_3$.

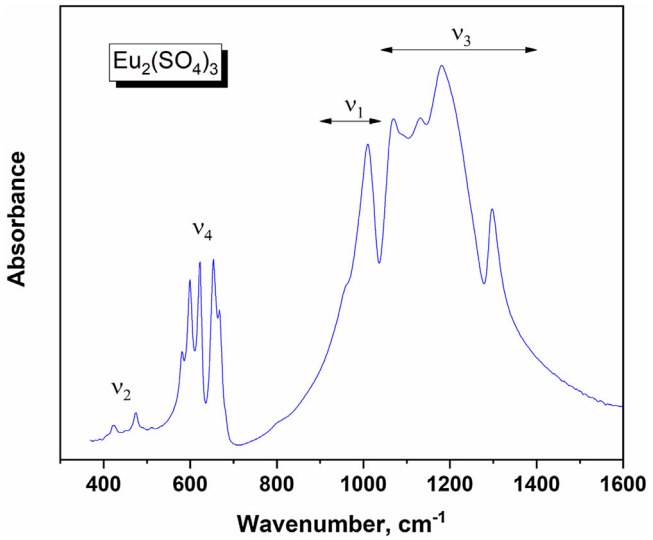

Fig. 7. The IR spectrum of $Eu_2(SO_4)_3$.

modes are Raman active, and A_u and B_u modes are infrared-active. According to the XRD data, the $Eu_2(SO_4)_3$ crystal structure contains two translationally independent SO_4 tetrahedra S1 and S2. Each ideal tetrahedral SO_4 group has four Raman-active (ν_1–ν_4) and two infrared-active (ν_3, ν_4) normal vibrations. The rules $\nu_3 > \nu_1$ and $\nu_4 > \nu_2$ are for the compounds with SO_4 tetrahedra [80]. In the case of isolated SO_4 groups, the asymmetric stretching ν_3 vibration can be observed around 1100 cm^{-1}, the symmetric stretching ν_1 vibration is positioned around 980 cm^{-1}, and bending ν_4 and ν_2 modes are observed in the region of 600 and 450 cm^{-1} [80,81]. The detailed symmetry classification of phonons of SO_4 tetrahedra in the $Eu_2(SO_4)_3{\cdot}8H_2O$ hydrate have been shown earlier [82]. The correlation diagrams between the free SO_4 groups of T_d symmetry, site symmetry and factor group symmetry of the unit cell in anhydrous $Eu_2(SO_4)_3$ are presented in Tables 3 and 4. It can be concluded that 12 Raman active modes can appear in the range of stretching vibrations. Three of them are SO_4 symmetric stretching and nine modes are asymmetric stretching modes. Two very strong Raman lines observed at 1026 and 1066 cm^{-1} (Figs. 6 and S4) can be interpreted as the symmetric stretching ones of SO_4 groups. The remaining lines in this region correspond to SO_4 asymmetric stretching vibrations. The IR bands in the range of 900–1040 cm^{-1} are symmetric stretching and, in the range of 1040–1400 cm^{-1}, they are asymmetric stretching of SO_4, as shown in Fig. 7.

The 550–700 cm^{-1} region of Raman and IR spectra is related to ν_4 bending vibrations. In this wavenumber range, at least seven modes can be resolved by the Raman spectra deconvolution (Fig. S5) and five bands can be observed in this region of IR spectra. In the 375–550 cm^{-1} region, six Raman lines related to the ν_2 modes of SO_4 can appear, and five peaks were resolved in the recorded spectrum shown in Fig. S6. The Raman spectrum measured in the case of excitation at 514.5 nm is shown in Figs. S7 and S8, and the additional peaks related to Eu^{3+}

Table 3
Correlation diagram between the T_d point symmetry, C_1 sites symmetry and the C_{2h} factor group symmetry for $S1O_4$ in $Eu_2(SO_4)_3$.

Wavenumber, cm^{-1} [80]	T_d Point group	C_1 Site symmetry	C_{2h} Factor group symmetry
983	A_1 (ν_1)	A	$A_g + A_u + B_g + B_u$
450	E(ν_2)	$2A$	$2A_g + 2A_u + 2B_g + 2B_u$
1105	F_2(ν_3)	$3A$	$3A_g + 3A_u + 3B_g + 3B_u$
611	F_2(ν_4)	$3A$	$3A_g + 3A_u + 3B_g + 3B_u$

Table 4
Correlation diagram between the T_d point symmetry, C_2 site symmetry and the C_{2h} factor group symmetry for $S2O_4$ in $Eu_2(SO_4)_3$.

Wavenumber, cm^{-1} [80]	T_d Point group	C_2 Site symmetry	C_{2h} Factor group symmetry
983	A_1 (ν_1)	A	$A_g + A_u$
450	E (ν_2)	$2A$	$2A_g + 2A_u$
1105	F_2 (ν_3)	$A + 2B$	$A_g + A_u + 2B_g + 2B_u$
611	F_2 (ν_4)	$A + 2B$	$A_g + A_u + 2B_g + 2B_u$

photoluminescence lines in the region of ν_2 bending modes can be clearly seen [28]. The broad bands detected at 733, 853, 935 and 1346 cm^{-1} are attributed to the Eu^{3+} photoluminescence, too (Fig. S8). The IR bands related to ν_2 bending vibrations are found in the range of 400–550 cm^{-1}. The Raman lines in the region of 100–275 cm^{-1} are related to translational and rotational modes of SO_4 tetrahedra, and the lattice modes are observed below 100 cm^{-1}. The obtained Raman spectra indicate the absence of water molecules in the sample. However, the weak bands related to H_2O vibrations exist in the IR spectrum (Fig. S9). This can be associated with the water absorption during the preparation of the tablets for the IR measurements.

The luminescence spectrum of $Eu_2(SO_4)_3$ obtained with the excitation wavelength of 394 nm is presented only by the bands which corresponded to the characteristic transitions of europium ion Eu^{3+} $^5D_0 \rightarrow {}^7F_J$ (J = 0–4): 580 nm $^5D_0 \rightarrow {}^7F_0$; 590 nm and 590 nm $^5D_0 \rightarrow {}^7F_1$; 614 nm $^5D_0 \rightarrow {}^7F_2$; 652 nm $^5D_0 \rightarrow {}^7F_3$; 697 nm $^5D_0 \rightarrow {}^7F_4$. The most intensive band maximized at 614 nm. The high resolution $Eu_2(SO_4)_3$ spectra recorded using a T64000 spectrometer and 514.5 nm excitation line are presented in Figs. 8 and 9, in comparison with reference crystal α-$Eu_2(MoO_4)_3$ [28]. The polycrystalline samples of both compounds were taken in equal amounts for these measurements. Corrections on the number density of Eu^{3+} ion and on the variation of absorption coefficient were not accounted for in view of the absence of the latter data. First of all, serious variations in the intensities distribution between $^5D_0 \rightarrow {}^7F_J$ manifolds, as well as the changes in the shapes of individual luminescent bands in $Eu_2(SO_4)_3$, with respect to α-$Eu_2(MoO_4)_3$, are pronounced. These variations, evidently, are due to the modification of the local environment of Eu^{3+} ions in a new crystalline structure of $Eu_2(SO_4)_3$, that have led to the change of the symmetry and the strength of the crystal field affecting the Eu^{3+} ion. Specifically, local environment of Eu ion in $Eu_2(SO_4)_3$ is featured by weaker violation of inversion symmetry in comparison with α-$Eu_2(MoO_4)_3$, in contrast, for example, to recent demonstration of symmetry reduction in different system of La_2O_3 nanoparticles doped by europium in the course of increasing of Eu content [83]. Comparing the intensities of magnetic dipole

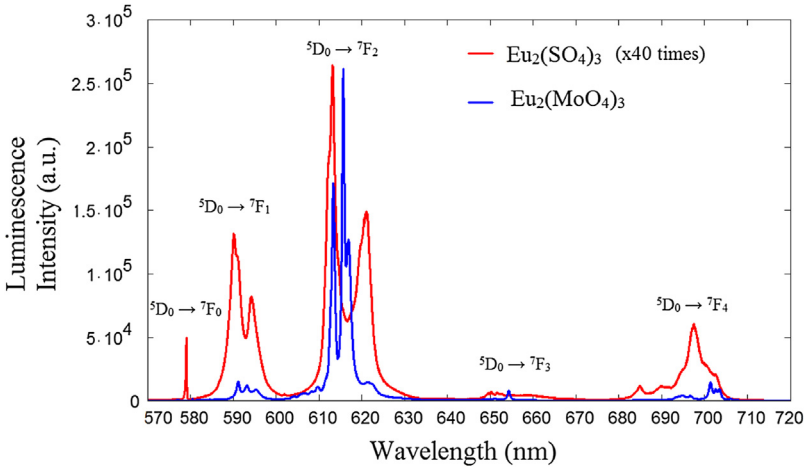

Fig. 8. High resolution luminescence spectra of $Eu_2(SO_4)_3$ (red, multiplied by 40) and of the reference crystal (α-$Eu_2(MoO_4)_3$) (blue) excited at 514.5 nm. (For interpretation of the references to color in this figure legend, the reader is referred to the web version of this article).

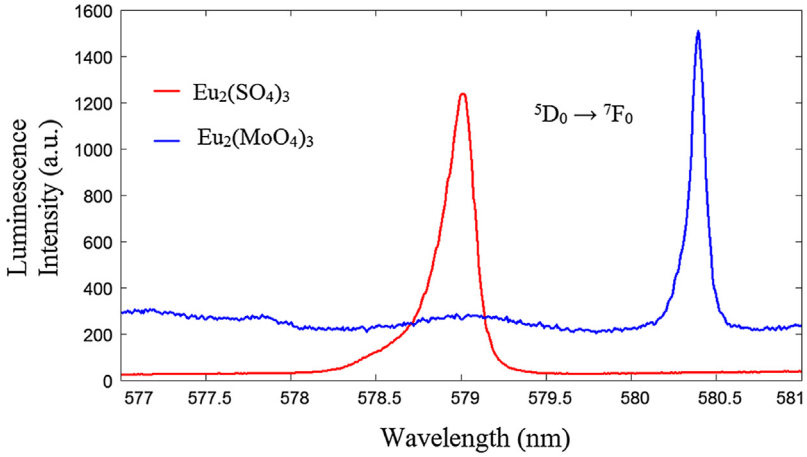

Fig. 9. High resolution luminescence spectra of $Eu_2(SO_4)_3$ (red) and of the reference crystal (α-$Eu_2(MoO_4)_3$) (blue) excited at 514.5 nm in the vicinity of ultranarrow $^5D_0 \rightarrow {}^7F_0$ transition. (For interpretation of the references to color in this figure legend, the reader is referred to the web version of this article).

transitions $^5D_0 \rightarrow {}^7F_1$, that are not affected by the parity violation induced by the local environment, we can deduce that the radiativeless relaxation of the $^5D_0$ state in $Eu_2(SO_4)_3$ is estimated as 5 times stronger than that in α-$Eu_2(MoO_4)_3$. The maximum luminescent band, namely, the hypersensitive one $^5D_0 \rightarrow {}^7F_2$, is 40 times weaker in the amplitude and 20 times weaker in the integral intensity in $Eu_2(SO_4)_3$ than that in $Eu_2(MoO_4)_3$, and this means, in addition to the influence of radiativeless losses, a smaller parity breaking effect of the crystal field in $Eu_2(SO_4)_3$. Oppositely, the ultranarrow $^5D_0 \rightarrow {}^7F_0$ line in $Eu_2(SO_4)_3$ is of equal amplitude with that in the reference crystal structure. Therefore, the breaking of the mirror symmetry of the Eu ion local environment in the sulfate crystal structure is considerably stronger than that in the molybdate crystal structure. These observations are somehow similar to those deduced from the investigation of another new crystalline structure with the Eu ion, namely, $Rb_3EuB_6O_{12}$ [34]. One can also note the blue shift of ultranarrow transition peak to 579 nm in $Eu_2(SO_4)_3$ associated with the substitution of molybdenum by sulfur in this new crystal structure.

Conclusions

In the present study, the structural and spectroscopic properties, and thermal stability of $Eu_2(SO_4)_3$ have been explored for the first time. The chemical precipitation route in hard acids was proposed for the synthesis of anhydrous $Eu_2(SO_4)_3$. It was found that $Eu_2(SO_4)_3$ crystallized in the monoclinic structure closely related to that of α-$Eu_2(MoO_4)_3$ and $Nd_2(SO_4)_3$. Consequently, the crystallization of the europium(III) sulfate in $Nd_2(SO_4)_3$ structural type allows supposing that all sulfates of the "light" Ln sulfates (La–Eu) crystallize in the monoclinic syngony with space group C2/*c*. Passing on to the sulfates of "heavy" Ln (Gd–Lu), the symmetry enhancement takes place up to the orthorhombic syngony with space group *Pbcn*. There is a strong possibility that the change of structural type will be realized through the morphotropic transition related to gadolinium sulfate. The luminescence measurements of anhydrous $Eu_2(SO_4)_3$ indicate that the radiativeless deexcitation of $^5D_0$ state in this crystal is estimated as 5 times stronger than that in closely structured α-$Eu_2(MoO_4)_3$. However, the peak luminescence at the hypersensitive $^5D_0 \rightarrow {}^7F_1$ transition is 40 times weaker, indicating a smaller effect of the parity breaking by the crystal field. At the same time, the ultranarrow $^5D_0 \rightarrow {}^7F_1$ transition luminescence in $Eu_2(SO_4)_3$ is of the same amplitude as that in α-$Eu_2(MoO_4)_3$, evidencing a stronger mirror symmetry violation at the europium ion site.

Acknowledgements

This work was supported by the Russian Foundation for Basic Research (16-52-48010, 17-52-53031). The equipments of the Collective Use Center — Kirensky Institute of Physics, Federal Research Center KSC Siberian Branch Russian Academy of Sciences [http://ccu.kirensky.ru/] was used.

Appendix A. Supplementary data

Supplementary data associated with this article can be found, in the online version, at https://doi.org/10.1016/j.jiec.2018.07.034.

References

[1] P.C. Burns, M.L. Miller, R.C. Ewing, Can. Mineral. 34 (4) (1996) 845.
[2] F.C. Hawthorne, S.V. Krivovichev, P.C. Burns, Rev. Mineral. Geochem. 40 (2000) 1.
[3] V. Ramanathan, P.J. Crutzen, J. Lelieveld, A.P. Mitra, D. Althausen, J. Anderson, M.O. Andreae, W. Cantrell, G.R. Cass, C.E. Chung, J. Geophys. Res. Atmos. 106 (D22) (2001) 28371.
[4] G.P. Anipsitakis, D.D. Dionysiou, Environ. Sci. Technol. 38 (13) (2004) 3705.
[5] K.D. Dermadis, E. Mavredaki, A. Stathoulopoulou, E. Neofotistou, C. Mantzaridis, Desalination 213 (1–3) (2007) 38.
[6] J.T. Anderson, C.L. Munsee, C.M. Hung, T.M. Phung, G.S. Herman, D.C. Johnson, J. F. Wager, D.A. Keszler, Adv. Funct. Mater. 17 (13) (2007) 2117.
[7] J.L. Arias, A. Neira-Carrillo, J.I. Arias, C. Escobar, M. Bodero, M. David, M.S. Fernabdez, J. Mater. Chem. 14 (14) (2004) 2154.
[8] Z. He, Z.M. Wang, C.H. Yan, CrystEngComm 7 (2005) 143.
[9] N.N. Golovnev, M.S. Molokeev, S.N. Vereshchagin, V.V. Atuchin, J. Coord. Chem. 68 (11) (2015) 1865.
[10] S.P. Sirotinkin, V.A. Efremov, L.M. Kovba, A.N. Pokrovsky, Kristallografiya 22 (6) (1977) 1272.
[11] S.P. Sirotinkin, A.N. Pokrovskii, Zh. Neorg. Khim. 27 (8) (1982) 2142.
[12] M.S. Wickleder, Z. Anorg. Allg. Chem. 625 (11) (1999) 1794.
[13] S.P. Sirotkin, A.N. Pokrovskii, L.M. Kovba, Vestnik Moskovskogo Universiteta Seriya 2 Khimiya 18 (4) (1977) 479.
[14] M.S. Wickleder, J. Alloys Compd. 303–304 (2000) 445.
[15] H.U. Hummel, E. Fischer, T. Fischer, P. Joerg, G. Pezzei, Z. Anorg. Allg. Chem. 619 (4) (1993) 805.
[16] M.S. Wickleder, Z. Anorg. Allg. Chem. 626 (6) (2000) 1468.
[17] S.P. Sirotinkin, A.N. Pokrovsky, L.M. Kovba, Kristallografiya 26 (2) (1981) 385.
[18] M.S. Wickleder, Z. Anorg. Allg. Chem 624 (8) (1998) 1347.
[19] S.P. Sirotinkin, A.N. Pokrovskii, L.M. Kovba, Zh. Neorg. Khim. 23 (4) (1978) 1139.
[20] M.S. Wickleder, Chem. Rev. 102 (6) (2002) 2011.
[21] Stuart J. Mills, Václav Petříček, Anthony R. Kampf, Regine Herbst-Imer, Mati Raundsepp, J. Solid State Chem. 184 (9) (2011) 2322.
[22] P.A. Tanner, Chem. Soc. Rev. 42 (12) (2013) 5090.
[23] Pinglu Shi, Zhiguo Xia, Maxim S. Molokeev, Victor V. Atuchin, Dalton Trans. 43 (2014) 9669.
[24] Xuebin Qiao, Hyo Jin Seo, J. Alloys Compd. 648 (2015) 809.
[25] Anjie Fu, Anxiang Guan, Fangfang Gao, Xiaoshan Zhang, Liya Zhou, Yingbin Meng, Haiman Pan, Opt. Laser Tchnol. 96 (2017) 43.
[26] Jiaxi Wang, Li Luo, Baoyu Huang, Jinqi He, Wei Zhang, Weiren Zhao, Jianqing Wang, Materials 11 (2) (2018) 297.
[27] O.D. Chimitova, V.V. Atuchin, B.G. Bazarov, M.S. Molokeev, Zh.G. Bazarova, Proc. SPIE 8771 (2013) 87711A.
[28] V.V. Atuchin, A.S. Aleksandrovsky, O.D. Chimitova, T.A. Gavrilova, A.S. Krylov, M.S. Molokeev, A.S. Oreshonkov, B.G. Bazarov, J.G. Bazarova, J. Phys. Chem. C 118 (28) (2014) 15404.
[29] A.M. Abakumov, V.A. Morozov, A.A. Tsirlin, J. Verbeeck, J. Hadermann, Inorg. Chem. 53 (2014) 9407.
[30] Haipeng Ji, Zhaohui Huang, Zhiguo Xia, Maxim S. Molokeev, Xingxing Jiang, Zheshuai Lin, Victor V. Atuchin, Dalton Trans. 44 (16) (2015) 7679.
[31] Dan Zhao, Fa-Xue Ma, Zhi-Qiang Wu, Lei Zhang, Wei Wei, Juan Yang, Rong-Hua Zhang, Peng-Fei Chen, Shan-Xuan Wu, Mater. Chem. Phys. 182 (2016) 231.
[32] Ali H. Reshak, Z.A. Alahmed, J. Bila, Victor V. Atuchin, Bair G. Bazarov, Olga D. Chimitova, Maxim S. Molokeev, Igor P. Prosvirin, Alexander P. Yelisseyev, J. Phys. Chem. C 120 (2016) 10559.
[33] Dan Zhao, Fa-Xue Ma, Bao-Zhong Liu, Yun-Chang Fan, Xue-Feng Han, Lie Zhang, Cong-Kui Nie, Z. Kristallogr. Cryst. Mater. 233 (2) (2018) 73.
[34] V.V. Atuchin, A.K. Subanakov, A.S. Aleksandrovsky, B.G. Bazarov, J.G. Bazarova, T.A. Gavrilova, A.S. Krylov, M.S. Molokeev, A.S. Oreshonkov, S.Yu. Stefanovich, Mater. Des. 140 (2018) 488.
[35] Yan Xu, Shaohua Ding, Xiefang Zheng, J. Solid State Chem. 180 (7) (2007) 2020.
[36] X. Zhang, Yu. Ma, H. Zhao, C. Jiang, Yu. Sun, Ya. Xu, J. Struct. Chem. 52 (5) (2011) 954.
[37] J.F. Lynch, C.J. Sachs, H.G. Brittain, Thermochim. Acta 109 (1987) 343.
[38] Yu.G. Denisenko, N.A. Khritokhin, O.V. Andreev, S.A. Basova, E.I. Sal'nikova, A.A. Polkovnikov, J. Solid State Chem. 255 (2017) 219.
[39] S. Geller, Acta Cryst. 10 (11) (1957) 713.
[40] Thanjavur Ramabhadran Sarangarajan, Krishnaswamy Panchanatheswaran, John N. Low, Cristopher Glidewell, Acta Crystallogr. E 60 (11) (2004) i142.
[41] D.Y. Wei, Y.Q. Zheng, Z. Kristallogr. New Cryst. Struct. 218 (2003) 299.
[42] Myung-Ho Choi, Min Kyung Kim, Vinna Jo, Dong Woo Lee, Il-Wun Shim, Kang Min Ok, Bull. Korean Chem. Soc. 31 (4) (2010) 1077.
[43] Lilli Paama, Ilkka Pitkänen, Jussi Valkonen, Eed Pärnoja, Harri Kola, Paavo Perämäki, Talanta 67 (5) (2005) 897.
[44] Victor V. Atuchin, Tatiana A. Gavrilova, Sergey A. Gromilov, Vitalii G. Kostrovsky, Lev D. Pokrovsky, Irina B. Troitskaia, R.S. Vemuri, G. Carbajal-Franco, C.V. Ramana, Cryst. Growth Des. 9 (4) (2009) 1829.
[45] N.N. Golovnev, M.S. Molokeev, S.N. Vereshchagin, V.V. Atuchin, J. Coord. Chem. 66 (23) (2013) 4119.
[46] Victor V. Atuchin, Ludmila I. Isaenko, Valery G. Kesler, Lei Kang, Zheshuai Lin, Maxim. S. Molokeev, Aleksander P. Yelisseyev, J. Phys. Chem. C 117 (2013) 7269.
[47] B.T. Sone, E. Minikandan, A. Gurib-Fakim, M. Maaza, J. Alloys Compd. 650 (2015) 357.
[48] Victor V. Atuchin, Nina F. Beisel, Eugeniy N. Galashov, Egor M. Mandrik, Maxim S. Molokeev, Aleksander P. Yelisseyev, Alexey A. Yusuf, Zhiguo Xia, ACS Appl. Mater. Interfaces 7 (2015) 26235.
[49] Faezeh Soofivand, Masoud Salavati-Niasari, Ceram. Int. 41 (2015) 14394.
[50] Chang Sung Lim, Aleksandr Aleksandrovsky, Maxim Molokeev, Aleksandr Oreshonkov, Victor Atuchin, Phys. Chem. Chem. Phys. 17 (2015) 19278.
[51] Maryam Ghiyasiyan-Arani, Maryam Masjedi-Arani, Masoud Salavati-Niasari, J. Mater.: Mater. Electron. 27 (2016) 4871.
[52] Maryam Ghiyasiyan-Arani, Maryam Masjedi-Arani, Davood Ghanbari, Samira Bagheri, Masoud Salavati-Niasari, Sci. Rep. 6 (2016) 25231.

[53] Abdoulaye Diallo, Bakang M. Mothudi, Elayaperumal Manikandan, Malik Maaza, J. Nanophoton. 10 (2) (2016) 026010.
[54] Fatemeh Mazloom, Maryam Masjedi-Arani, Maryam Ghiyasiyan-Arani, Masoud Salavati-Niasari, J. Mol. Liq. 214 (2016) 46.
[55] Maryam Ghiyasiyan-Arani, Maryam Masjedi-Arani, Masoud Salavati-Niasari, J. Mol. Liq. 216 (2016) 59.
[56] Nicolay N. Golovnev, Maxim S. Molokeev, Maxim K. Lesnikov, Irina V. Sterkhova, Victor V. Atuchin, J. Mol. Struct. 1149 (2017) 367.
[57] Maryam Ghiyasiyan-Arani, Masoud Salavati-Niasari, Sara Naseh, Ultrason. Sonochem. 39 (2017) 494.
[58] E.N. Galashov, V.V. Atuchin, T.A. Gavrilova, I.V. Korolkov, Y.M. Mandrik, A.P. Yelisseyev, Zhiguo Xia, J. Mater. Sci. 52 (22) (2017) 13033.
[59] Ali Salehabadi, Masoud Salavati-Niasari, Maryam Ghiyasiyan-Arani, J. Alloys Compd. 745 (2018) 789.
[60] Maryam Ghiyasiyan-Arani, Masoud Salavati-Niasari, Maryam Masjedi-Arani, Fatemeh Mazloom, J. Mater. Sci.: Mater. Electron. 29 (2018) 474.
[61] Nicolay N. Golovnev, Maxim S. Molokeev, Maxim K. Lesnikov, Victor V. Atuchin, J. Phys. Org. Chem. 31 (3) (2018) 3773.
[62] Reza Mahassel, Azam Sobhani, Mojgan Goudarzi, Masoud Salavati-Niasari, J. Alloys Compd. 753 (2018) 615.
[63] Reza Mahassel, Azam Sobhani, Masoud Salavati-Niasari, Mojgan Goudarzi, Spectrochim. Acta A: Mol. Biomol. Spectrosc. 204 (2018) 232.
[64] Haipeng Ji, Zhaohui Huang, Zhiguo Xia, Maxim S. Molokeev, Xingxing Jiang, Zheshuai Lin, Victor V. Atuchin, Dalton Trans. 44 (16) (2015) 7679.
[65] Bruker AXS TOPAS V4: General Profile and Structure Analysis Software for Powder Diffraction Data — User's Manual, Bruker AXS, Karlsruhe, Germany, 2008.
[66] A.A. Savina, V.V. Atuchin, S.F. Solodovnikov, Z.A. Solodovnikova, A.S. Krylov, E. A. Maximovsky, M.S. Molokeev, A.S. Oreshonkov, A.M. Pugachev, E.G. Khaikina, J. Solid State Chem. 225 (2015) 53.
[67] B.N. Kuznetsov, N.Yu. Vasilieva, A.V. Levdansky, A.A. Karacharov, A.S. Krylov, E. V. Mazurova, G.N. Bondarenko, V.A. Levdansky, A.S. Kazachenko, J. Bioorg. Chem. 43 (7) (2017) 722.
[68] V.A. Blatov, A.P. Shevchenko, D.M. Proserpio, Cryst. Growth Des. 14 (7) (2014) 3576.
[69] W.H. Baur, Acta Crystallogr. B 30 (5) (1974) 1195.
[70] P.O. Andreev, E.I. Sal'nikova, O.V. Andreev, Yu.G. Denisenko, I.M. Kovenskii, Inorg. Mater. 53 (2) (2017) 200.
[71] I.A. Razumkova, A.N. Boiko, O.V. Andreev, S.A. Basova, Russ. J. Inorg. Chem. 62 (4) (2017) 418.
[72] O.V. Andreev, I.A. Razumkova, A.N. Boiko, J. Fluorine Chem. 207 (2018) 77.
[73] E.E. Ferg, D.G. Billing, A.M. Venter, Solid State Sci. 64 (2017) 13.
[74] Shoufeng Xue, Wenyuan Wu, Xue Bian, J. Rare Earths 35 (11) (2017) 1156.
[75] Jia Peng, Xiaobei Zheng, Tingting Qiu, Size Gao, Yuxia Liu, Lan Zhang, J. Fluorine Chem. 193 (2017) 106.
[76] G.C. Fitzgibbon, E.J. Huber Jr., C.E. Holley Jr., J. Chem. Thermodyn. 4 (3) (1972) 349.
[77] F.D. Rossini, Proc. Natl. Acad. Sci. 16 (11) (1930) 694.
[78] J.E. Kunzler, W.F. Giauque, J. Am. Chem. Soc. 74 (14) (1952) 3472.
[79] Ingo Hartenbach, Thomas Schleid, Z. Anorg. Allg. Chem. 628 (9–10) (2002) 2171.
[80] K. Nakamoto, Infrared and Raman Spectra of Inorganic and Coordination Compounds, 6th ed., Wiley, New York, 2009.
[81] W.W. Rudolph, G. Irmer, G.T. Hefter, Phys. Chem. Chem. Phys. 5 (2003) 5253.
[82] S. Ram, J. Raman Spectrosc. 18 (8) (1987) 537.
[83] Hao Suo, Xiaoqi Zhao, Zhiyu Zhang, Rui Shi, Yanfang Wu, Jinmeng Xianga, Chongfeng Guo, Nanoscale 10 (2018) 9245.